Gravity Balancing Flexure Springs for an Assistive Elbow Orthosis

Martin Tschiersky, Edsko E. G. Hekman, *Member, IEEE*, Dannis M. Brouwer, and Just L. Herder, *Member, IEEE*

***Abstract*—In this paper, we propose a flexure spring based gravity compensation device which provides assistance to lift the forearm. Three different spring designs are obtained and evaluated. The synthesis method to obtain these is explained in detail and an experimental evaluation validates the desired gravity balancing properties. It is found that in comparison to a flexure spring with constant thickness, a variable thickness distribution along the spring leads to a drastic reduction of its width, which amounts to 81 % in the presented case, and offers an energy to weight ratio that is 94 % higher. Employing a nested spring design further increases the storable elastic energy of the variable thickness design by 145 % through utilization of the otherwise unused space within the original spring envelope. A proof-of-concept prototype is built to illustrate a practical implementation. The presented synthesis method provides a tool to obtain gravity balancing flexure springs that offer a promising solution for the design of assistive devices which aim to be both wearable and inconspicuous.**

***Index Terms*—Gravity balancing, wearable device, assistive orthosis, arm support, flexure spring.**

I. Introduction

GRAVITY balancing supports for the upper limb are used to facilitate functional movements of the arm. The main group associated with the use of gravity balancing arm supports are people suffering from neuromuscular disorders. Due to muscular weakness their ability to execute activities of daily living (ADLs) is severely impeded which leads to a large dependency on external help in the form of caregivers. Furthermore, social participation is often heavily affected. Assistive devices using gravity balancing principles can play a key role in restoring the ability to execute ADLs independently and enhancing social participation [1], [2].

Manuscript received April 18, 2019; revised June 2, 2019; accepted June 18, 2019. Date of publication July 23, 2019; date of current version August 21, 2019. This paper was recommended for publication by Associate Editor D. Accoto and Editor P. Dario upon evaluation of the reviewers' comments. This project has received funding from the European Union's Horizon 2020 research and innovation programme under grant agreement No. 688857 (SoftPro). *(Corresponding author: Martin Tschiersky.)*

M. Tschiersky and D. M. Brouwer are with the Chair of Precision Engineering, University of Twente, 7500 AE Enschede, The Netherlands (e-mail: m.tschiersky@utwente.nl).

E. E. G. Hekman is with the Department of Biomechanical Engineering, University of Twente, 7500 AE Enschede, The Netherlands.

J. L. Herder is with the Department of Precision and Microsystems Engineering, Delft University of Technology, 2628 CD Delft, The Netherlands.

This paper has supplementary downloadable material available at http://ieeexplore.ieee.org, provided by the authors. These files expand on the content of the paper and are intended to allow better understanding. A CAD file is added to enable reproduction. This material is 67.8 Mb in size.

Digital Object Identifier 10.1109/TMRB.2019.2930341

A. State of the Art

Within the domain of assistive devices two categories can be distinguished: end-effectors and exoskeletons. These can be further subdivided by method of actuation [3], [4]. While most of the commercially available arm supports are passive end-effector devices [3], the benefits of wearable exoskeletons are evident, as they allow for close alignment to the body, offer a more natural range of motion, allow for independent balancing of the upper arm and forearm, and enable increased mobility for both ambulatory users as well as wheelchair-bound users [1], [3], [5], [6]. A significant growth of upper-limb exoskeletons occurred in the last decades [7]. Yet, remarkably, the majority of upper-limb exoskeletons have never been used in daily life by their intended target populations [3]. Numerous reasons can be found to explain why potential target groups refrain from using upper-limb exoskeletons outside of clinical settings. In terms of system acceptability, these can be classified as a lack of either functional acceptability or social acceptability [8]. In order to achieve high functionality and biomechanical compatibility a trend towards an ever increasing technical complexity can be observed [7]. However, an increase in functionality does not necessarily correspond to an improved usability or usefulness for the user. As is generally observed by the academic community, the cost-benefit ratio associated with the use of current assistive devices is in most cases unfavorable [1], [2], [3], [4], [7], [8]. The most critical issue, as indicated by some authors, is the lack of social acceptability due to appearance. Thus arose the demand to make future devices inconspicuous, for example, by making them wearable underneath clothing [1], [8].

In the light of these considerations and given the present state-of-the-art of actuation and energy storage technology, we argue that the most promising solutions are currently to be found in passive wearable exoskeletons with spring-based gravity compensation. The number of devices which are designed to assist ADLs and feature these attributes, however, is very small. To the author's knowledge only four such devices exist at this point of time. The WREX [2], [5] and the A-Gear [9] are devices that support both upper arm and forearm against gravity. The SpringWear [10], [11] applies gravity compensation to the upper arm. The Wilmer elbow orthosis [12] supports the forearm.

B. Research Approach

With the exception of the Wilmer elbow orthosis, which is wearable underneath clothing, critique towards the above mentioned devices mainly concerns their inadequate weight, size and conspicuity. Common features of these devices are the use of rigid link mechanisms and rubber bands, which are used to store potential energy. While rubber bands, loaded in tension, offer a very high specific energy, they rely on a rigid structure to which they attach. Without this structure the spring forces would induce inadmissible levels of shear to the skin.

In the broader field of robotics many spring-based gravity balancing mechanisms have been devised. However, in most cases these also use linear extension and compression springs in combination with rigid mechanisms [13].

In order to build energy storing elements, i.e., springs, which do not induce high shear forces at their attachment points, we intend to explore the utilization of large stroke bending deformation for storing elastic strain energy. We hypothesize that by doing so we will be able to reduce the size of the frame and ultimately be able to refrain from using rigid linkages entirely. This aims to address the problems of the aforementioned assistive devices regarding their weight, size and conspicuity.

C. Scope

In the scope of this paper we design an elbow orthosis featuring a flexure spring that undergoes large deflections and balances the forearm against gravity when the upper arm maintains a low elevation angle. In previous work by Cheng *et al.* [14], [15] it was shown that such flexure springs can be synthesized and used to balance a planar linkage, representing the upper arm and forearm. Similar work outside the scope of assistive devices was conducted by Radaelli and Herder [16], [17], [18], where beam shapes have been synthesized that are used for general gravity balancing purposes. However, in all cases the resulting spring designs turn out to be large in respect to the amount of torque or force which they can deliver.

Therefore, as the first step towards our goal, this study does not yet attempt to minimize the shear forces exerted by the spring, but concentrates on finding ways to increase the specific energy and energy density of the spring, as these are fundamental key factors to make the use of such elements feasible in wearable devices.

The core of this study is the synthesis and experimental evaluation of three spring designs. The first spring, though different in topology and shape, is comparable to the design shown by Cheng *et al.* [15], featuring a constant cross-section. It is consequently suffering from similar shortcomings. The synthesis method is extended, however, to additionally optimize the thickness distribution along the spring. Thereby, a second design is obtained which features major improvements in terms of its size to energy ratio. Furthermore, it enables concentric nesting of additional spring elements. This leads to the third design in which, by utilizing the otherwise unused space within the original spring envelope, the energy density is further increased.

These two novel approaches in the field – variable thickness distribution and concentric nesting – provide the theoretical framework to build gravity balancing flexure springs which can be smaller and lighter than the above mentioned comparable predecessors.

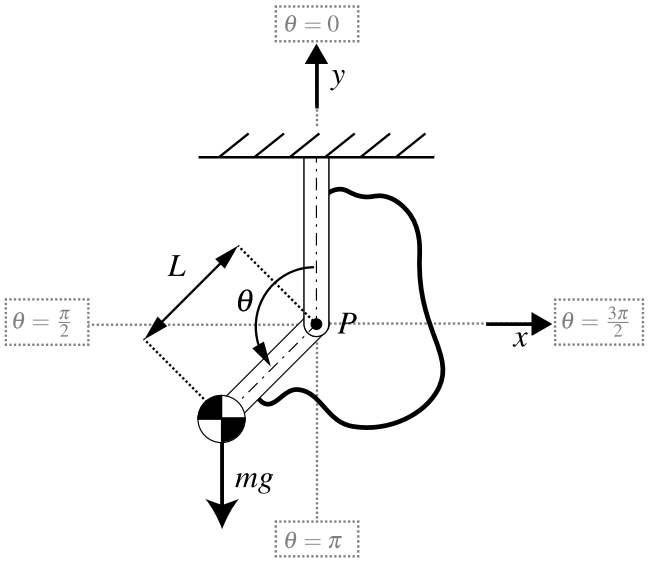

Fig. 1. Model topology at position $\theta = 3\pi/4$. The bold black solid line represents an arbitrary compliant beam. The black dashed-dotted lines depict the linkage axes, the gray dotted lines the coordinate axes with the respective angles indicated at their ends. The bold black dot shows the location of pivot P coinciding with the origin of the Cartesian space.

D. Structure

The main focus of this paper is on conveying the synthesis method by which the three spring designs were obtained. This is elaborated on in detail in the *Synthesis* section which follows this introduction. In order to verify the presented synthesis method a technical validation is conducted in a test bench environment, described in the *Experiment* section. The outcomes of both synthesis and experiment are shown in the *Results* section and are critically reflected upon in the *Discussion* section. In addition, an early proof-of-concept prototype is shown to illustrate the practical applicability. In the *Conclusion* section we concisely recapitulate the contents of this paper and attempt to put its contribution into the broader research context.

II. Synthesis

In this section the synthesis method is described by which desired beam geometries and their respective dimensions are obtained.

A. Topology

We suppose that the forearm can be represented by a point mass m on a lever with length L rotating around a fixed point P representing the elbow joint. In order to statically balance this system a moment has to be generated that will counteract the moment generated by the point mass under the influence of gravity. To this end, a compliant curved beam which acts as a spring is clamped to the forearm link on one end and to the fixed world, representing the upper arm, on the other end. An idealized physical model topology can be seen in Figure 1.

B. Task Definition

An angular displacement of the lever in the range of $\theta = [0 \dots \pi]$ rad is investigated, as this fully covers the range of motion of the human elbow joint. Ideally, the energy is exchanged reversibly between the spring and the mass, such that the total energy of the system remains constant for any angle θ. Since the potential energy of the mass is maximum at $\theta = 0$ and the gravity forces are supported by the rigid linkage in this position, it is chosen as the initial position such that no pre-stress is required.

Our approach is to achieve mechanical equilibrium for the entire deflection range of θ. As a sufficient condition in this case, only the moments around the pivot P are observed. The moment generated by the mass under the influence of gravity is

$$M_g = mgLsin(\theta) \tag{1}$$

where M_g is the gravity moment and g is the gravitational acceleration constant. Consequently, the balancing moment M_b is the additive inverse of M_g, thus

$$M_b = -M_g = -mgLsin(\theta). \tag{2}$$

C. Parametrization

The spring is considered mathematically as a beam. In order to optimize the beam, its geometry is described by an appropriate vector of design parameters. The parameter vector $\mathbf{x}$ is divided into three parts, of which the first two parts describe the shape of the neutral beam axis, and the third part determines the thickness distribution along the beam.

To obtain the shape of the neutral axis of the beam, a control polygon formed by an array of control points is interpolated using the piecewise biarc Hermite spline interpolation function *rscvn()* from the MATLAB Curve Fitting Toolbox. The start-point (x_0, y_0) and end-point (x_n, y_n) of the control polygon are directly described in terms of Cartesian coordinates. Since in its initial configuration both endpoints are defined to coincide with the vertical coordinate axis at $x = 0$, only the y-components $[y_0, y_n]$ are explicitly specified as variables in the parameter vector $\mathbf{x}$. The positions of all intermediate points are determined using a linkage chain formulation as proposed by Radaelli and Herder [17]. To this end, the lengths l and relative angles φ of all links in the linkage chain are stored in the second part of the parameter vector $\mathbf{x}$. As described by Radaelli and Herder [17], [18], this formulation enables efficient control of the distances between control points and of the relative angles between links through the use of bounds during the optimization. The parametrization of the neutral axis is depicted in Figure 2.

In order to prescribe a stiffness variation along the beam an array of two or more thickness modifiers *tm* is appended to the parameter vector $\mathbf{x}$. This yields the complete parameter vector of the form

$$\mathbf{x} = [[y_0, y_n], [l_1, \varphi_1, \dots, l_n, \varphi_n], [tm_1, \dots, tm_n]]. \tag{3}$$

D. Discretization & Analysis

To evaluate design parameter sets defined by $\mathbf{x}$ during the optimization routine numerical analyses are conducted using the flexible multibody dynamics software package

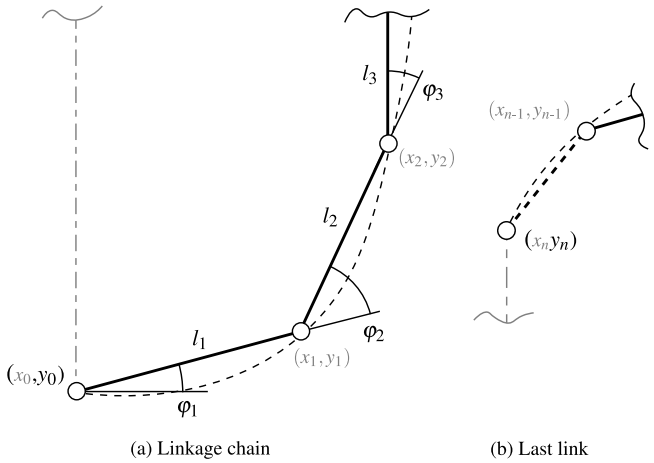

(a) Linkage chain (b) Last link

Fig. 2. Parametrization of the neutral axis through linkage chain formulation. Black values indicate explicit parameters. Grey values show the respective implicit coordinates. The solid line depicts the control polygon, the weak dashed line the Hermite spline interpolation, the bold dashed line the last link of the control polygon which is not part of the linkage chain and the gray dashed-dotted line the vertical axis at $x = 0$.

SPACAR [19]. The mechanism is modeled using finite planar beam elements. Levers are modeled as rigid, massless beams. An extension of the two-node beam element is used, to model the flexible, pre-curved beams [20].

Bending deformations of a single beam element in SPACAR are modeled using a cubic polynomial shape function that interpolates between its two nodes. Furthermore, each beam element possesses constant cross-sectional properties. Thus, in order to model a complex shaped beam with changing thickness it has to be discretized by multiple beam elements.

The nodal coordinates of these beam elements are obtained by linear subdivision of the neutral axis spline function according to its basic interval $\Psi = [\psi_0 = 0 \dots \psi_{max}]$ (see Figure 3-a). However, the value of ψ is not directly proportional to the arc-length of the spline. As a result the beam element nodes are generally not evenly distributed along the neutral axis.

The thickness modifiers *tm* are linearly interpolated across these nodes, to obtain a refined thickness modifier tm_r for each node (see Figure 3-b). The median of two refined thickness modifiers tm_r at both end-nodes of a beam element determines the discretized thickness modifier tm_d for that element. To obtain the corresponding actual thickness t of that beam element, the dimensionless thickness modifier tm_d is multiplied with a thickness base value t_b, which provides the absolute scale (see Figure 3-c).

E. Shape Optimization

The goal of the shape optimization is to find an ideal beam shape and stiffness distribution along the beam, which leads to optimal gravity balancing behavior while observing multiple constraints. The Genetic Algorithm function *ga()* from the MATLAB Global Optimization Toolbox is used for solving the minimization problem.

To obtain an optimal parameter set $\mathbf{x}^*$ we consider a minimization problem for the cost function $f(\mathbf{x})$. The function $f(\mathbf{x})$ comprises the objective $\boldsymbol{\delta}$ and a set of penalties $\mathbf{p}$,

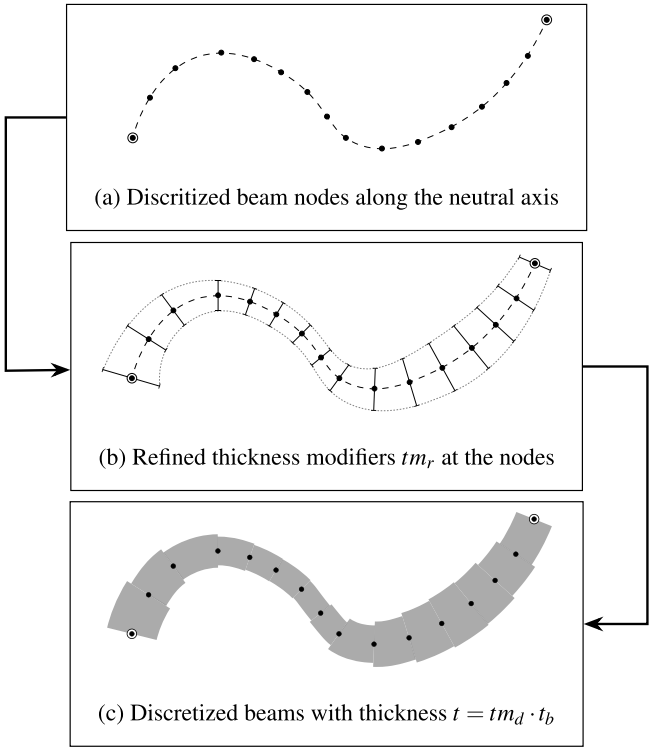

Fig. 3. Three-step model discretization procedure.

which are multiplied by penalty coefficients k_p.

$$f(\mathbf{x}) = \boldsymbol{\delta} + k_p \mathbf{p} \tag{4}$$

The problem is subject to lower bounds $\mathbf{b_l}$ and upper bounds $\mathbf{b_u}$. Furthermore, linear inequality constraints $\mathbf{c_l}$ and non-linear inequality constraints $\mathbf{c_{nl}}$ apply.

The objective is to find a beam design that creates a negative sine-shaped moment curve as the lever travels from $\theta = 0$ to $\theta = \pi$ rad. Assuming isotropic material properties, the shape of that moment curve is solely determined by the dimensionless beam shape and the relative stiffness distribution, as described by $\mathbf{x}$. Therefore, the other design variables: actual in-plane size (i.e., scale), actual beam thickness, beam width and material properties can be determined separately and are chosen arbitrarily for the shape optimization. These remaining variables are obtained in a subsequent dimensioning step, described in Section II-F, that determines a mechanical feasible design based on desired metrics, such as the desired absolute moment amplitude and in-plane size, while considering maximum and minimum values of the beam thickness and beam width, respectively. This two-step procedure is used to reduce the amount of design variables that are optimized simultaneously, in order to minimize the design space for the computationally demanding shape optimization.

The discrete moment curve $\dot{M}$ generated by a certain spring design is determined in simulation and normalized by its absolute maximum amplitude $|\dot{M}|_{max}$. The objective $\boldsymbol{\delta}$ is defined as the mean absolute error between the value of this normalized moment response and the value of the ideal moment characteristic $-sin(\theta)$ at each angle θ_k.

$$\boldsymbol{\delta} = \sum_{k=1}^{\bar{n}} \frac{|\ \dot{M}_k/|\dot{M}|_{max} + sin(\theta_k)\ |}{\bar{n}} \tag{5}$$

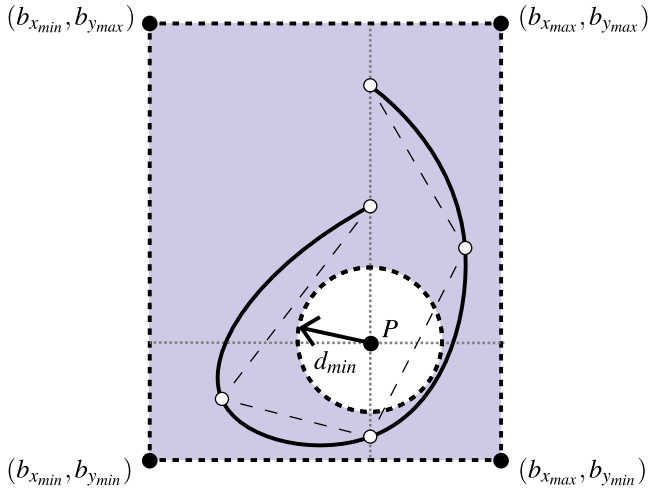

Fig. 4. Spatial constraints of the neutral axis spline. The bold black dashed lines show the borders of the feasible region, which is indicated by the shaded area. The solid black line shows the neutral axis spline. The spline and its control points must lie within the feasible region. The control polygon of the spline, drawn as the weak dashed lines, can pass through infeasible regions.

where k is a discrete load step and $\bar{n}$ is the total number of load steps at which the objective is evaluated.

Two linear constraints are used to limit both the sum of the lengths of the linkage chain links l and the relative angles φ, avoiding an excessive beam length and loops. The maximum permitted total length and angle are represented by $Ł_{max}$ and Φ_{max}, respectively.

$$\mathbf{c_l}_{(1)} = |\sum_{i=1}^{n} l_i| - Ł_{max} \tag{6}$$

$$\mathbf{c_l}_{(2)} = |\sum_{i=1}^{n} \varphi_i| - \Phi_{max} \tag{7}$$

Seven non-linear constraints are used of which one is treated as an option. The first non-linear constraint limits the distance between the end of the linkage chain (x_{n-1}, y_{n-1}) and the end-node of the control polygon (x_n, y_n). The maximum distance $ł_{max}$ is equal to the upper boundary $\mathbf{b_u}_l$ of the link lengths l.

$$\mathbf{c_{nl}}_{(1)} = \sqrt{(x_n - x_{n-1})^2 + (y_n - y_{n-1})^2} - ł_{max} \tag{8}$$

The remaining non-linear constraint checks are carried out at discrete points $(\hat{x}_i, \hat{y}_i)$, $i \in [1, \ldots, \hat{n}]$ on the beam neutral axis, given by the spline interpolation. A feasible region is defined by a rectangle with lower bounds $[b_{x_{min}}, b_{y_{min}}]$ and upper bounds $[b_{x_{max}}, b_{y_{max}}]$.

$$\mathbf{c_{nl}}_{(2,3)} = [b_{x_{min}} - \hat{x}_i, \quad b_{y_{min}} - \hat{y}_i] \tag{9}$$

$$\mathbf{c_{nl}}_{(4,5)} = [\hat{x}_i - b_{x_{max}}, \quad \hat{y}_i - b_{y_{max}}] \tag{10}$$

Thereby, mainly the position of the neutral axis in relation to the rotary joint is controlled. For an overview of the spatial constraints refer to Figure 4.

To detect self-intersections of the neutral axis in the undeformed state an iterative procedure is conducted. Two line segments L_1 and L_2 are considered. L_1 spans the distance between $(\hat{x}_i, \hat{y}_i)$ and $(\hat{x}_{i+1}, \hat{y}_{i+1})$, while L_2 spans the distance between $(\hat{x}_j, \hat{y}_j)$ and $(\hat{x}_{j+1}, \hat{y}_{j+1})$. For each line segment L_1 in the interval $i = [1 \ldots \hat{n} - 2]$ potential intersections with all consecutive line segments L_2 in the interval $j = [i{+}1 \ldots \hat{n} - 1]$

are determined. First the x-component of the intersection point $I_{(i,j)}$ of the two straight lines collinear with the line segments L_1 and L_2, respectively, are determined.

$$\begin{aligned} I_{x(i,j)} &= \frac{\mathsf{a}-\mathsf{b}}{\mathsf{c}-\mathsf{d}}, \\ \mathsf{a} &= (\hat{x}_i\hat{y}_{i+1} - \hat{y}_i\hat{x}_{i+1})(\hat{x}_j - \hat{x}_{j+1}), \\ \mathsf{b} &= (\hat{x}_i - \hat{x}_{i+1})(\hat{x}_j\hat{y}_{j+1} - \hat{y}_j\hat{x}_{j+1}), \\ \mathsf{c} &= (\hat{x}_i - \hat{x}_{i+1})(\hat{y}_j - \hat{y}_{j+1}), \\ \mathsf{d} &= (\hat{y}_i - \hat{y}_{i+1})(\hat{x}_j - \hat{x}_{j+1}) \end{aligned} \tag{11}$$

Subsequently, a logic operation determines whether the intersection lies within both intervals L_1 and L_2. The result is stored in the matrix $n_{\times(i,j)}$.

$$\begin{aligned} n_{\times(i,j)} &= \begin{cases} 1, & \text{if} \quad \mathsf{e} \wedge \mathsf{f} \quad \leq 0 \\ 0, & \text{else} \end{cases} \\ \mathsf{e} &= (I_{x(i,j)} - \hat{x}_i)(I_{x(i,j)} - \hat{x}_{i+1}), \\ \mathsf{f} &= (I_{x(i,j)} - \hat{x}_j)(I_{x(i,j)} - \hat{x}_{j+1}) \end{aligned} \tag{12}$$

Since the segments are linear it is sufficient to only consider the x-components. The sum of all elements in $n_{\times(i,j)}$ yields the total number of intersections $\mathsf{n}_\times$. As self-intersections are not admissible, the limit value is zero. Thus, the respective constraint is

$$\mathbf{c_{nl}}_{(6)} = \mathsf{n}_\times = \sum_{i=1}^{\hat{n}-2} \sum_{j=i+1}^{\hat{n}-1} n_{\times(i,j)} \tag{13}$$

The last nonlinear constraint is optional. It ensures, that the neutral axis encloses the rotary pivot P while maintaining a minimum distance d_{min}. First, the MATLAB function *inpolygon()* is used to determine, if the polygon of all points $(\hat{x}_i, \hat{y}_i)$, $i = [[1, \ldots, \hat{n}] \rightarrow 1]$ encloses the rotary pivot P at $(0, 0)$. The result is stored in the Boolean variable Ξ, where $\Xi = 1$ indicates the joint being inside and $\Xi = 0$ it being outside the polygon. Next, the minimum distance between the polygon vertices and the pivot P is determined and depending on Ξ subtracted, respectively added to d_{min}. Thus,

$$\mathbf{c_{nl}}_{(7)} = \begin{cases} d_{min} + \min\sqrt{\hat{x}_i^2 + \hat{y}_i^2}, & \text{if} \quad \Xi = 0 \\ d_{min} - \min\sqrt{\hat{x}_i^2 + \hat{y}_i^2}, & \text{if} \quad \Xi = 1 \end{cases} \tag{14}$$

Two soft constraints are integrated into the cost function $f(\mathbf{x})$ as penalties $\mathbf{p}$, which are multiplied by a large penalty coefficient $k_p = 10^5$ and added to the objective $\boldsymbol{\delta}$. They are used to avoid dedicated runs of the computationally expensive SPACAR simulation for the evaluation of non-linear constraints.

The first of these soft constraints limits the self-intersections for the entire deflection range. Analog to the prior introduced self-intersection constraint $\mathbf{c_{nl}}_{(6)}$ for the undeformed state, a self-intersection test is performed at every load step k. In this case, the evaluated line segments correspond to the positions of the beam element nodes given by the SPACAR simulation. The sum of all self-intersections for all load steps $k = [1 \ldots \bar{n}]$ yields the score $\bar{\mathsf{n}}_\times$, which shall equal zero. The respective penalty is

$$\mathbf{p}_{(1)} = \bar{\mathsf{n}}_\times = \sum_{k=1}^{\bar{n}} \sum_{i=1}^{\hat{n}-2} \sum_{j=i+1}^{\hat{n}-1} n_{\times(i,j,k)} \tag{15}$$

The second soft constraint limits relative stress concentrations along the beam, which are expressed by the ratio between the maximum stress in the most stressed beam element and the average maximum stress that each beam element endures during one load cycle.

Each planar beam element has three discrete deformation modes e, which are each associated with a respective generalized stress σ. These deformation modes are elongation (e_1, σ_1) and bending (e_2, σ_2), (e_3, σ_3) at each end-node, respectively.

The penalty $\mathbf{p}_{(2)}$ is obtained by first separately evaluating the maximum absolute generalized stress per deformation mode which each beam element i endures throughout all load steps k.

$$\sigma_{(e,i)_{max}} = \max|\sigma_{(e,i,k)}| \quad \forall \quad k \in [1, \ldots, \bar{n}] \tag{16}$$

Then, the maximum stress per deformation mode, for all load steps is determined as

$$\sigma_{(e)_{max}} = \max|\sigma_{(e,i)_{max}}| \quad \forall \quad i \in [1, \ldots, \dot{n}] \tag{17}$$

Analogously, the mean per deformation mode is

$$\sigma_{(e)_{mean}} = \sum_{i=1}^{\dot{n}} \frac{|\sigma_{(e,i)_{max}}|}{\dot{n}} \tag{18}$$

The ratio between the maximum and the mean for each deformation mode is computed, and the highest ratio out of these yields the value λ.

$$\lambda = \max \frac{\sigma_{(e)_{max}}}{\sigma_{(e)_{mean}}} \qquad \forall \quad e \in [e_1, e_2, e_3] \tag{19}$$

If λ exceeds a predefined limit λ_{max}, then the difference yields Λ which equals the penalty $\mathbf{p}_{(2)}$.

$$\mathbf{p}_{(2)} = \Lambda = \begin{cases} \lambda - \lambda_{max} & \text{if} \quad \lambda - \lambda_{max} > 0 \\ 0 & \text{if} \quad \lambda - \lambda_{max} \leq 0. \end{cases} \tag{20}$$

F. Computation

Optimizations are conducted according to Section II-E using two sets of optimization parameters, **Set A** and **Set B**, that define the bounds $\mathbf{b}$, constraints $\mathbf{c}$, and penalties $\mathbf{p}$. Both parameter sets are shown in Table III in the Appendix. The key difference between the two sets is to be found in tm_{min}, the lower bound of the thickness modifiers tm, and the specification of d_{min}, the minimum distance to the pivot. When applying **Set A** the beam is optimized using a constant thickness and without constraining the beam to enclose the pivot P. In contrast, when applying **Set B** the beam thickness can vary between 0.2 and 1 times the thickness base value t_b and it is constrained to enclose P by enforcing $\mathbf{c_{nl}}_{(7)}$.

Subsequent to the shape optimization, a dimensioning procedure is conducted for each set of optimization parameters, respectively. First, a desired footprint size of the spring is defined and the corresponding ideal beam thickness base value t_b^* is determined. The desired footprint is described by a bounding box with prescribed height h_s and width w_s. A uniform scale factor s is determined such that the neutral line of the beam coincides tangentially with the inside of the bounding box. For this given in-plane size of the spring, the optimal beam base thickness t_b^* is defined as the value of t_b which, when multiplied with the discretized thickness modifiers tm_d

to obtain the actual thickness t along the beam, results in a maximum simulated von Mises stress σ_{mises} that equals a target stress $\mathring{\sigma}$, defined as the tensile strength σ_t divided by a factor of safety FOS. The objective $\boldsymbol{\eta}$ for this unconstrained optimization problem is

$$\boldsymbol{\eta} = |\sigma_{mises} - \mathring{\sigma}|, \quad \mathring{\sigma} = \frac{\sigma_t}{FOS} \tag{21}$$

The problem is solved with the MATLAB *fminbnd()* command, using the dimensioning parameters shown in Appendix Table IV. Next, the ideal out-of-plane beam width w_b^* is determined, which is defined as the value of w_b at which the amplitude of the moment curve a matches the requested amplitude a^*. Since the moment amplitude is linearly proportional to the out-of-plane width w_b, the optimal value w_b^* can be analytically determined from any out-of-plane width $\tilde{w_b}$ and its corresponding moment amplitude $\tilde{a}$ through

$$w_b^* = \tilde{w_b}\,\frac{a^*}{\tilde{a}} \tag{22}$$

The dimensioning is done for the material properties of PA 2200, as provided by the manufacturer data sheets [21], [22]. They can be found in Appendix Table V. Furthermore, limitations of the laser sintering process are considered. For both the dimensioning procedure and the numerical evaluation, the weight of the beam itself is taken into account.

G. Nesting

As the variable thickness beam (**Set B**) encloses the pivot P, it allows the creation of the spring design **Set C** in which multiple scaled versions of the same beam design are nested in an array of parallel beams arranged concentrically around the pivot P. Each beam in this compound structure shares the same shape parameters as the variable thickness beam defined by **Set B**. However, for each beam the thickness base value t_b is determined separately according to its scale factor s. For comparability, the dimensions of the outer beam are chosen to be identical with the original variable thickness beam and the width of all beams is chosen to be equal. The minimum distance between the beams is set to approximately 0.8 mm, in order to avoid fusing of the beams during laser sintering, and the smallest beam is determined by the minimum manufacturable beam thickness of 0.4 mm.

H. Performance Metrics

Gravity balancing quality, expressed in the objective $\boldsymbol{\delta}$, is considered to be the main performance metric in the scope of this paper, as it represents the fundamental function of the spring. However, for further comparison of the different spring designs secondary performance metrics are considered. These are the specific strain energy ε in respect to the fully deflected state, as well as the energy density ω in respect to the occupied bounding box volume during deflection V_Δ.

The total strain energy U that is stored in the spring in its fully deflected state is determined from the respective SPACAR simulation. The mass m is derived from CAD models. Division of U by m yields the specific energy ε of the spring, which can be used as a measure of the material utilization efficiency. The bounding box volume of the cumulative volume V_Δ that is occupied by the spring during a full deflection cycle is determined by multiplying the beam width w_b with the corresponding envelope area A_Δ. The latter is obtained from generating the convex hull of the point cloud formed by all beam element nodes, that have been superimposed for all load steps of the SPACAR simulation. Division of U by V_Δ yields the energy density ω, which can be used as a measure of the space utilization efficiency.

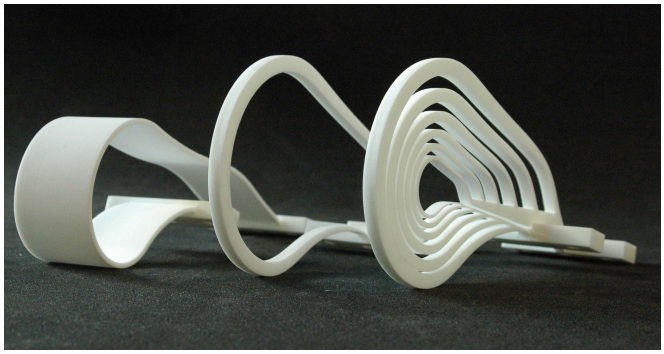

Fig. 5. Specimens, from left to right: **Set A**, **Set B**, **Set C**.

III. Experiment

A. Test Specimen

Specimens with smooth surfaces are obtained through further beam refinement. This is done in order to avoid stress concentrations at the transition between two discrete thicknesses. The refinement process is equivalent to increasing the number of beam elements in the simulation. Convergence studies showed that numerical results only change marginally when using more than the 50 beam elements, which are used for the dimensioning and for generating the computational results.

The physical test specimen are modeled such that the beam elements transition into large bodies (74x20x10 mm) at each end, which are used to mount specimen onto the test bench. For the nested spring design, extensions from these bodies connect to all parallel beams. The test specimens are made via plastic laser sintering on a EOS Formiga P110 using PA 2200, which is based on a polyamide 12.

Refer to Figure 5 for a comparison of the specimens and to Figure 6 to see the fixation to the test bench.

B. Test Setup

The experimental test setup, which is used to validate the simulation results is shown in Figure 6. The frame is built using 40x40 mm aluminum profiles and 3 mm steel plate, mounted on a 25 mm thick aluminum optical plate. The profiles form a box shaped frame, which is closed on top by two traverse profiles and supported on the left side by two triangular sections. The box frame is closed to the left and the right by steel plates. Between the two steel plates a rotating lever made from 10 mm thick aluminum is supported on each side by a roller bearing mounted in the respective steel plate, held in place by housings made from polylactide (PLA) polymer. Above the rotational axis a transverse beam connects both plates and serves as a rigid interface to the frame.

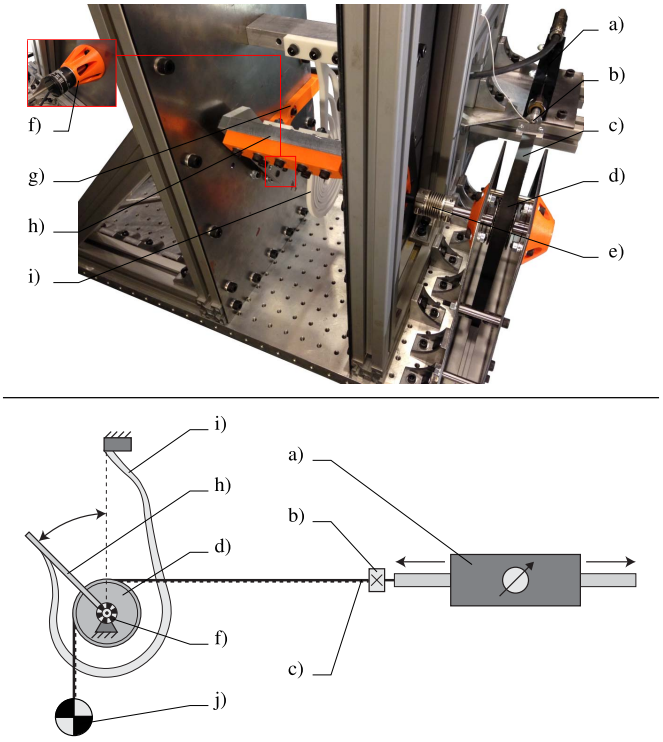

Fig. 6. Experimental setup: a) linear motor, b) force sensor, c) timing belt, d) timing pulley, e) bellows coupling, f) encoder (mounted to the opposite side), g) lever homing end-stop, h) lever, i) specimen, j) counter-mass.

The test specimens are clamped to the lever on one side and to the traverse beam to the other side, using M6 screws. A short lever extension made from PLA is used to compensate for the geometry changes between specimens. To the left side, the lever is connected via a rigid coupling to a YUMO E6B2-CWZ3E digital quadrature encoder. The encoder is mounted on the steel plate using a PLA mount. To the right side, the lever connects to a timing pulley via a bellows coupling. The pulley is again supported by two roller bearings mounted to two opposing steel plates, using PLA housings. The plates are connected to each other by bolts that run through steel tubes that act as spacers. Both plates are fixed to the optical plate via aluminum profiles.

A timing belt runs over the pulley, from which it extends horizontally to one side and vertically downward to the other side. At the horizontal end the belt is connected to a ME-Meßsysteme KM10z load cell. The load cell is mounted to its other side to a LinMot P01-23x160H-HP linear motor for actuation. The linear motor is fixed to a steel plate, which connects to the box shaped frame via aluminum profiles. At the downward end of the belt a counter-mass is attached, which provides the required belt tension for two-way actuation.

Electrically, the linear motor is connected to a LinMot B1100-VF-HC linear motor driver, which is connected to a PC via the RS-232 serial port. The force sensor is connected to a ME-Meßsysteme GSV-11H 010-5/20/2 measuring amplifier. The amplifier and the digital encoder both connect to a National Instruments BNC-2110 adapter, that sends the signals to a National Instruments PCI-6221 multifunction I/O device. The linear motor is controlled with command tables using the proprietary software LinMot-Talk. Sensor read-outs are performed using Simulink Real-Time.

C. Data Acquisition

Prior to every measurement, the lever performs a homing procedure using the end-stop bracket to set the initial motor position and encoder angle. The measurements begin at an initial inclination to avoid static indetermination at the upright vertical position due to friction in the system. From that initial angle the lever moves to the upright vertical position ($\theta = 0$), to the downright vertical position ($\theta = \pi$), and back to the upright vertical position ($\theta = 0$), which marks the end of the measurement. The measurement data are obtained at a constant angular velocity of $\frac{\pi}{40}$ rad/s and a data acquisition rate of 55 Hz for **Set A** and **Set B** and $\frac{\pi}{80}$ rad/s and 105 Hz for **Set C**. The force sensor signal is filtered in post-processing using a moving average filter with a window size of 110 and 105 samples, respectively. For each beam the angle-moment characteristic is measured with and without the beam being mounted. The difference between both measurements yields the presented spring characteristic.

A target angle-moment characteristic is defined as

$$\mathring{M} = -\mathring{a}sin(\theta) \ , \tag{23}$$

where the factor $\mathring{a}$ is equal to the maximum absolute amplitude of the mean spring characteristic. Subtracting the target characteristic from the spring characteristic, yields the balanced angle-moment characteristic. For a movie showing the compound spring specimen (**Set C**) performing one load cycle on the test setup, please refer to supplementary file 5.

IV. Results

A. Computational Results

For all presented results the respective optimizations exited normally and without any constraint violations. Multiple runs for each set of optimization parameters were performed with different optimizer settings, in order to avoid local minima and to increase the chance of finding the global optimum.

The sets of optimized parameters for **Set A** and **Set B** are shown in Table VI and the dimensions are given in Table VII in the Appendix. The dimensions of all six beams that constitute the compound beam **Set C** are shown in Appendix Table VIII. A significant difference between the dimensions is the out-of-plane width, which is 34.3 mm for **Set A** and 6.6 mm for **Set B** and **Set C**.

The final beam geometries are shown in Figure 7 for different deflected states.

The corresponding moment response curves are shown in Figure 8. Note that, while the balancing behavior of **Set C** is qualitatively equivalent to **Set B**, the absolute amplitude of the moment curve has increased to 2.45 Nm. For a version of Figure 7 using the jet color map and animations of the deflecting beams, please refer to the supplementary files 1 - 4.

A comparison of the performance metrics of all spring designs is given in Table I.

The balancing errors for **Set A**, **Set B** and **Set C** as determined by the normalized mean absolute error (δ) are 2 %,

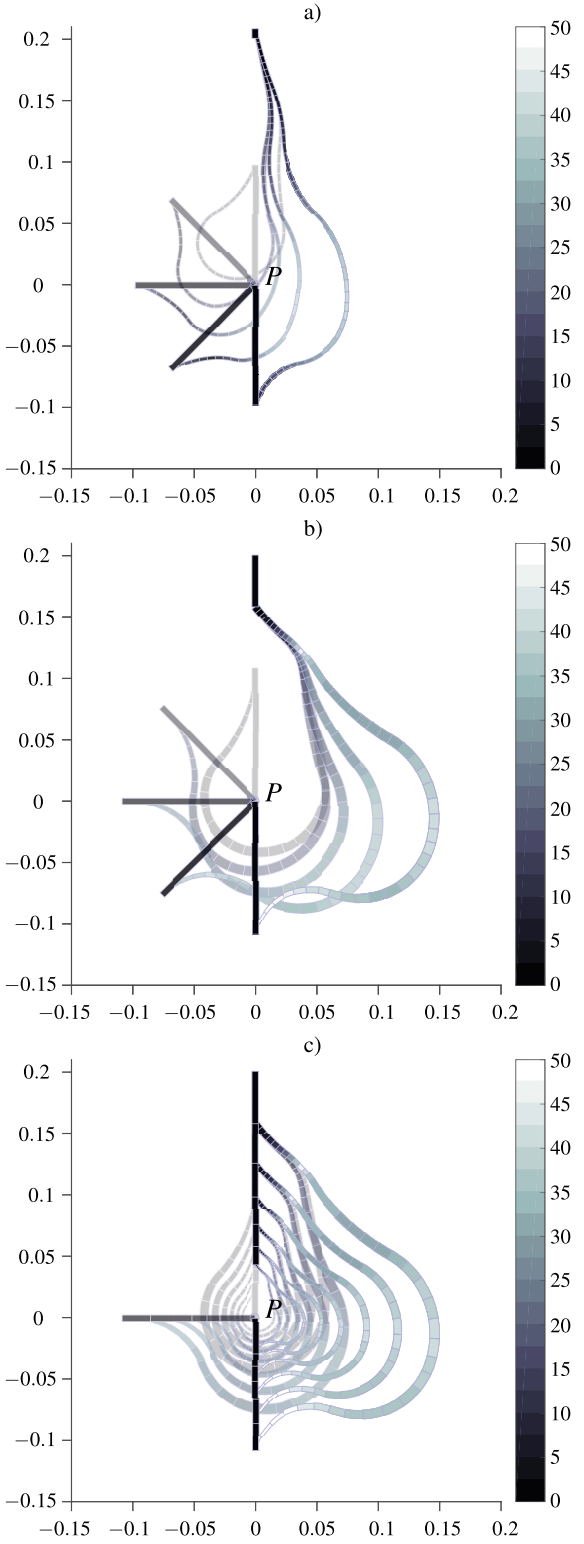

Fig. 7. Deflection of the different beam designs. From top to bottom a): the constant thickness beam **Set A**, b): the variable thickness beam **Set B** and c): the compound variable thickness beam **Set C**. Transparency decreases linearly from 80 % to 0 % with increasing deflection. Axes in m, color scale in MPa (true color at 0 % transparency, i.e., full deflection).

1.5 % and 1.7 %, respectively. Furthermore, it can be seen that the specific energy ε in the variable thickness designs is 94-96 % higher compared to the constant thickness design. In addition, the energy density ω increases by 277 % from

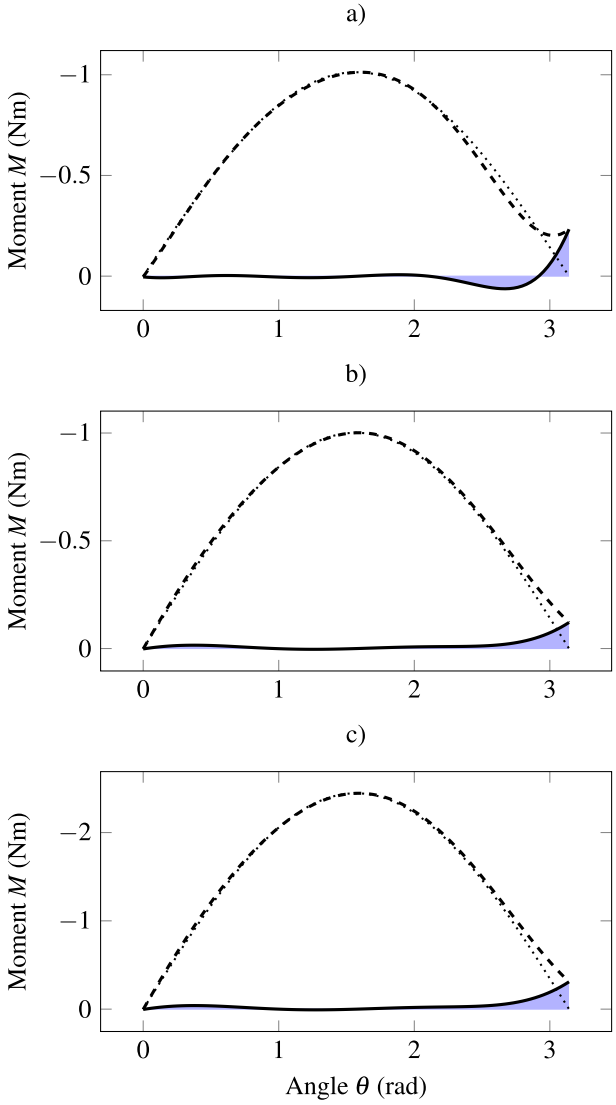

Fig. 8. Moment response curves. From top to bottom a): **Set A**, b): **Set B** and c): **Set C**. The dashed line depicts the moment generated by the beam. The dotted line indicates the ideal angle-moment characteristic. The solid line shows the balanced moment, which results from adding the load moment (inverse of the ideal moment) to the beam moment. The shaded area between the solid line and zero depicts the mean absolute error, i.e., the objective. This diagram shows that in all three cases the gravity load is nearly completely balanced throughout the entire range of motion.

constant to variable thickness, and further by 145 % from single beam to compound design, constituting a total increase of 823 % from **Set A** to **Set C**.

B. Experimental Results

The results in Figure 9 all show a pronounced hysteresis field. The balancing error between the mean spring characteristic and the target spring characteristic, listed in Table II, is expressed in terms of the mean absolute error (MAE), the root mean square error (RMSE) and their normalized counterparts, NMAE respectively NRMSE. Normalization is achieved through devision by the target amplitude $\mathring{a}$. The balancing error according to the NMAE, which has the same definition as the objective $\boldsymbol{\delta}$, is 8.8 %, 5 % and 10.9 % for **Set A**, **Set B** and **Set C**, respectively.

TABLE I
PERFORMANCE METRICS

Par.	Unit	**Set A**	**Set B**	**Set C**
δ	-	**0.02004**	**0.01526**	**0.01659**
U	J	2.02905	2.04874	5.01264
m	kg	0.03156	0.01642	0.03987
ε	J/kg	64.2917	124.771	125.725
A_Δ	cm^2	319.899	447.576	447.576
V_Δ	cm^3	1094.79	293.565	293.565
ω	J/cm^3	0.00185	0.00698	0.01708

TABLE II
EXPERIMENTAL RESULTS

Par.	Unit	**Set A**	**Set B**	**Set C**
MAE	Nm	0.09628	0.05105	0.27291
NMAE(δ)	-	0.08757	0.05008	0.10906
RMSE	Nm	0.16450	0.06640	0.33337
NRMSE	-	0.14960	0.06514	0.13322

V. DISCUSSION

A. Synthesis Method

While the original rationale to use the thickness as an additional design parameter was to gain more design freedom in order to allow for concentric stacking of beams, the results suggest that doing so, in addition, leads to an increased specific energy and energy density of the spring. The variable thickness approach appears particularly well suited to reduce the out-of-plane width. The variable thickness spring design **Set B** features a width, that is 81 % smaller in respect to the constant thickness counterpart **Set A**. However, along with the decrease in width the in-plane area covered by the variable thickness spring during deflection A_Δ increased by 40 %. The nesting approach, on the other hand, appears well suited to reduce that in-plane area. By elimination of the outer beam of the presented nested design **Set C** the in-plane area can be reduced by 37 %, while maintaining a load capacity which is still higher than that of the original variable thickness spring **Set B**. Therefore, a promising direction for future work appears to specifically optimize springs towards an increased stack density of nested beams.

Still, the number of investigated designs is low and increasing the specific energy and the energy density were not immediate optimization objectives in this study. The complex relationship between the admitted amount of thickness variation, the resulting beam shape and achievable number of nested beams as well as their specific influence on gravity balancing quality, specific energy and energy density remain unclear.

B. Experimental Validation

The quality of the experimental validation is impaired by the choice of the spring material. The specimen made from laser sintered PA 2200 exhibit significant viscoelastic behavior. This negatively influences the validity of the presented results. Aside from the pronounced hysteresis, shown in Figure 9, a positive correlation between the stiffness and the testing speed was observed. Furthermore, performing consecutive experiments led to a rapid degradation of the desired mechanical behavior.

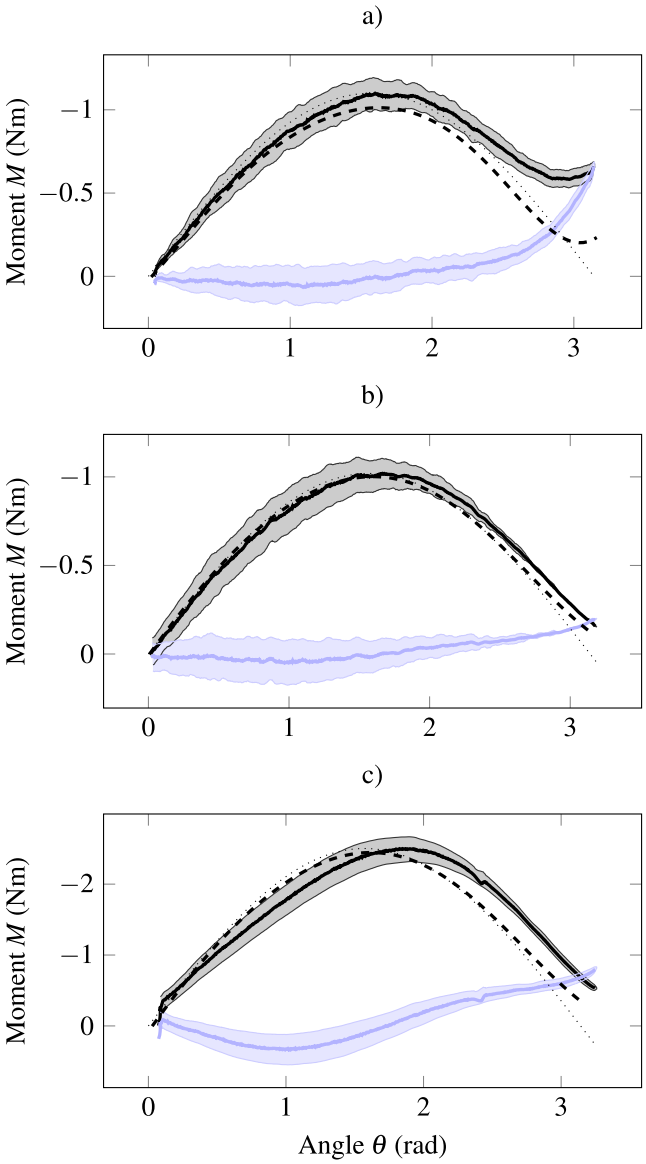

Fig. 9. Experimental results for the beam specimens. From top to bottom a): **Set A**, b): **Set B** and c): **Set C**. The target angle-moment characteristic is depicted by the black thin dotted line. The thin black solid line depicts the moment generated by the beam specimen. The shaded area in-between indicates the hysteresis, while the thick black solid line depicts the mean. The balanced moment characteristic is depicted analogously in light blue. The corresponding simulation result is shown by the thick dashed line (compare also with Figure 8). This diagram shows that for all specimens the gravity load is mostly balanced throughout the entire range of motion with general trend of a slightly increasing deviation towards full deflection at π rad.

C. Application

Based on a Wilmer elbow orthosis [12] and the **Set C** spring design a proof-of-concept prototype of an Assistive Elbow Orthosis (ÆOs) is built, which is shown in Figure 10. This prototype illustrates the close lateral alignment of the spring to the orthosis and thus to the body of the wearer. A lateral positioning appears conceptually advantageous, as in this configuration the spring does not impede tactile sensation on the backside of the arm, e.g., when resting the elbow

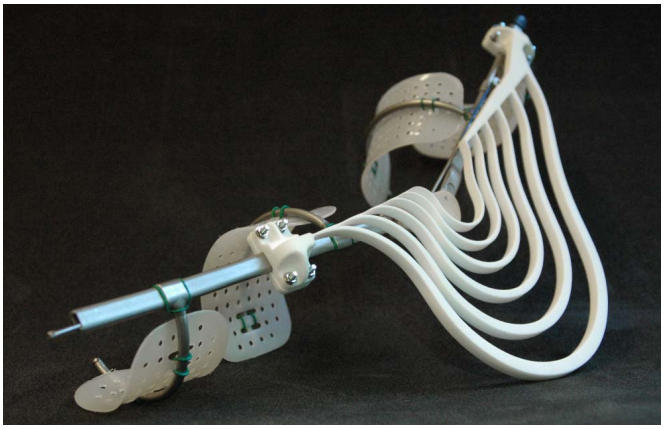

Fig. 10. Wearable proof-of-concept prototype of the Assistive Elbow Orthosis (ÆOs). It consists of a Wilmer elbow orthosis [12] and a laser-sintered PA 2200 spring based on **Set C**, illustrating the lateral spring alignment. The orthosis is locked in the extended position.

and forearm on an object. The total weight of the device is 0.213 kg.

However, since the spring design from **Set C** has not been adapted for increased wearability, its in-plane size remains too large to be worn underneath clothing. In future devices, a trade-off between using beams with smaller in-plane size and larger out-of-plane width may lead to a more favorable design. Dividing the effective out-of-plane width between two springs that are worn on either side of the arm may be done to mitigate lateral protrusion from the body. In addition, other materials may be investigated to further reduce the size of the spring and to avoid mechanical degradation due to creep and stress relaxation. For a movie showing the wearable prototype used by a healthy subject, refer to supplementary file 6. For a CAD model of the wearable spring shown in Figure 10, refer to supplementary file 7.

Extending the presented synthesis method to the other joints of the human upper and lower limb seems largely feasible. In many cases, the same spring designs as presented in this paper can be used for that purpose. However, a few limitations and design challenges arise.

Due to the planar design of the spring it can only balance a single rotational degree of freedom. Proper alignment of the rotational axis of the spring to the balanced degree of freedom in the joint has to be ensured. This can pose a challenge for joints that have multiple degrees of freedom, large ranges of motion and shifting rotation axes.

Since collision with the wearer is disregarded and the nesting procedure attempts to use the entire space within the spring, a lateral alignment is always assumed.

Due to its passive nature, one side of the spring needs to maintain a fixed orientation relative to the gravity vector. Balancing of multiple joints across body segments can be achieved by decoupling mechanisms as shown in [15]. However, the technical embodiment may lead to and increased complexity, size and weight of the device and may impede the mobility of the affected joints.

For the shoulder joint specifically, a design with a fully extended initial lever position appears more favorable, as to avoid the fixed side of the spring being above the shoulder.

TABLE III
BOUNDS, CONSTRAINT VALUES AND PENALTY COEFFICIENTS

Item	Parameter	Unit	**Set A**	**Set B**
$\mathbf{b_l}_{y_0}$	$y_{0_{min}}$	m	0.1	0.1
$\mathbf{b_u}_{y_0}$	$y_{0_{max}}$	m	0.2785	0.2785
$\mathbf{b_l}_{y_n}$	$y_{n_{min}}$	m	0.05	0.05
$\mathbf{b_u}_{y_n}$	$y_{n_{max}}$	m	0.2835	0.2835
$\mathbf{b_l}_{l}$	l_{min}	m	0.005	0.005
$\mathbf{b_u}_{l}$	l_{max}	m	0.5	0.5
$\mathbf{b_l}_{\varphi}$	φ_{min}	rad	$-2/3\pi$	$-2/3\pi$
$\mathbf{b_u}_{\varphi}$	φ_{max}	rad	$2/3\pi$	$2/3\pi$
$\mathbf{b_l}_{tm}$	tm_{min}	-	1	0.2
$\mathbf{b_u}_{tm}$	tm_{max}	-	1	1
$\mathbf{c_l}_{(1)}$	$Ł_{max}$	m	3	3
$\mathbf{c_l}_{(2)}$	Φ_{max}	rad	$8/3\pi$	$8/3\pi$
$\mathbf{c_{nl}}_{(1)}$	$ł_{max}$	m	0.5	0.5
$\mathbf{c_{nl}}_{(2)}$	$b_{x_{min}}$	m	-0.05	-0.05
$\mathbf{c_{nl}}_{(3)}$	$b_{y_{min}}$	m	-0.05	-0.05
$\mathbf{c_{nl}}_{(4)}$	$b_{x_{max}}$	m	0.01	0.01
$\mathbf{c_{nl}}_{(5)}$	$b_{y_{max}}$	m	0.3285	0.3285
$\mathbf{c_{nl}}_{(6)}$	$\mathsf{n}_{\times max}$	-	0	0
$\mathbf{c_{nl}}_{(7)}$	d_{min}	m	-	0.05
$\mathbf{p}_{(1)}$	λ_{max}	-	2	2
$\mathbf{p}_{(1)}$	$k_{p_{(1)}}$	-	10^5	10^5
$\mathbf{p}_{(2)}$	$\bar{\mathsf{n}}_{\times max}$	-	0	0
$\mathbf{p}_{(2)}$	$k_{p_{(2)}}$	-	10^5	10^5

Implementing this would require changes to the topology and task definition, which is left for future study.

VI. CONCLUSION

This study is the first to explore variable thickness beam profiles as well as concentric nesting of beams in the context of gravity balancing flexure springs. Utilizing the presented synthesis method, three spring designs are obtained, which exhibit gravity balancing behavior. The error in balancing quality is $\leq$2 % in simulation and 5-11 % in experiment. By employing a variable thickness profile along the beam, the out-of-plane width is reduced drastically, by 81 % in the presented case, and the energy to weight ratio is increased by 94 % in comparison to the constant thickness design. Furthermore, this novel approach provides the additional design freedom to enable concentric nesting of multiple differently-sized beams. The resulting nested spring design exhibits a 145 % increase of storable elastic energy compared to its single beam counterpart, while preserving the same outer dimensions.

These results show that employing the presented design methodology, gravity balancing springs can be obtained which ultimately feature a smaller size and a lower weight than comparable predecessors. In the context of passive gravity balancing exoskeletons the presented nested spring design offers a promising solution to increase wearability and decrease conspicuity, which are important criteria to promote the adoption of assistive devices for daily use. The proof-of-concept prototype illustrates a practical implementation.

APPENDIX

See Tables III–VIII.

TABLE IV
DIMENSIONING PARAMETERS

Parameter	Unit	Value
h_s	m	0.2
w_s	m	0.2
$t_{b_{min}}$	m	0.0004
$t_{b_{max}}$	m	0.05
FOS	-	1.2

TABLE V
MATERIAL PARAMETERS OF PA 2200 (PA12) PERFORMANCE 1.0, AT ROOM TEMPERATURE

Property	Parameter	Unit	Value
Tensile Modulus	E	MPa	1700
Shear Modulus	G	MPa	800
Tensile Strength	σ_t	MPa	50
Density	ρ	kg/m^3	930

TABLE VI
OPTIMIZED SHAPE PARAMETERS

$\mathbf{x} =$			
Parameter	Unit	**Set A**	**Set B**
y_0	m	0.222087	0.192382
y_n	m	0.104909	0.131396
l_1	m	0.097847	0.082104
φ_1	rad	-1.354998	-0.92193
l_2	m	0.129454	0.185152
φ_2	rad	-0.630883	-0.94523
tm_1	-	1	0.799912
tm_2	-	1	0.463851
tm_3	-	-	0.999999
tm_4	-	-	0.999999
tm_5	-	-	0.200226

TABLE VII
DIMENSIONS: SINGLE BEAMS

Parameter	Unit	**Set A**	**Set B**
h	m	0.200000	0.200000
w	m	0.048781	0.044597
s	-	0.934411	0.824749
t_b	m	0.002765	0.007867
w_b	m	0.034223	0.006559

TABLE VIII
DIMENSIONS: COMPOUND BEAM

Par.	Unit	**Set C**					
		c_1	c_2	c_3	c_4	c_5	c_6
h	m	0.2000	0.1588	0.1240	0.0955	0.0733	0.0543
w	m	0.0446	0.0354	0.0276	0.0213	0.0164	0.0121
s	-	0.8247	0.6550	0.5114	0.3938	0.3024	0.2241
t_b	m	0.0079	0.0062	0.0049	0.0038	0.0029	0.0021
w_b	m	0.0066					

ACKNOWLEDGMENT

The content of this publication is the sole responsibility of the authors. The European Commission or its services cannot be held responsible for any use that may be made of the information it contains.

REFERENCES

[1] A. G. Dunning and J. L. Herder, "A review of assistive devices for arm balancing," in *Proc. IEEE 13th Int. Conf. Rehabil. Robot. (ICORR)*, Jun. 2013, pp. 1–6.

[2] T. Rahman *et al.*, "Passive exoskeletons for assisting limb movement," *J. Rehabil. Res. Develop.*, vol. 43, no. 5, pp. 583–590, Aug./Sep. 2006.

[3] L. A. van der Heide, B. van Ninhuijs, A. Bergsma, G. J. Gelderblom, D. J. van der Pijl, and L. P. de Witte, "An overview and categorization of dynamic arm supports for people with decreased arm function," *Prosthetics Orthotics Int.*, vol. 38, no. 4, pp. 287–302, 2014.

[4] P. Maciejasz, J. Eschweiler, K. Gerlach-Hahn, A. Jansen-Troy, and S. Leonhardt, "A survey on robotic devices for upper limb rehabilitation," *J. Neuroeng. Rehabil.*, vol. 11, no. 1, p. 3, Jan. 2014.

[5] T. Haumont *et al.*, "Wilmington robotic exoskeleton: A novel device to maintain arm improvement in muscular disease," *J. Pediatric Orthopaedics*, vol. 31, no. 5, 2011, Art. no. e44-9.

[6] A. G. Dunning, M. M. H. P. Janssen, P. N. Kooren, and J. L. Herder, "Evaluation of an arm support with trunk motion capability," *J. Med. Devices*, vol. 10, no. 4, 2016, Art. no. 044509.

[7] R. A. R. C. Gopura, D. S. V. Bandara, K. Kiguchi, and G. K. I. Mann, "Developments in hardware systems of active upper-limb exoskeleton robots: A review," *Robot. Auton. Syst.*, vol. 75, pp. 203–220, Jan. 2016.

[8] O. Plos, S. Buisine, A. Aoussat, F. Mantelet, and C. Dumas, "A universalist strategy for the design of assistive technology," *Int. J. Ind. Ergonomics*, vol. 42, no. 6, pp. 533–541, 2012.

[9] P. N. Kooren *et al.*, "Design and pilot validation of A-gear: A novel wearable dynamic arm support," *J. Neuroeng. Rehabil.*, vol. 12, no. 1, p. 83, Sep. 2015.

[10] J. Chen and P. S. Lum, "Spring operated wearable enhancer for arm rehabilitation (springwear) after stroke," in *Proc. 38th Annu. Int. Conf. IEEE Eng. Med. Biol. Soc. (EMBC)*, Aug. 2016, pp. 4893–4896.

[11] J. Chen and P. S. Lum, "Pilot testing of the spring operated wearable enhancer for arm rehabilitation (springwear)," *J. Neuroeng. Rehabil.*, vol. 15, no. 1, p. 13, Mar. 2018.

[12] D. H. Plettenburg, "The WILMER elbow orthosis," in *Proc. IEEE 10th Int. Conf. Rehabil. Robot.*, Jun. 2007, pp. 1031–1035.

[13] V. Arakelian, "Gravity compensation in robotics," *Adv. Robot.*, vol. 30, no. 2, pp. 79–96, 2016.

[14] Z. Cheng, S. Foong, D. Sun, and U. X. Tan, "Algorithm for design of compliant mechanisms for torsional applications," in *Proc. IEEE/ASME Int. Conf. Adv. Intell. Mechatron.*, Jul. 2014, pp. 628–633.

[15] Z. Cheng, S. Foong, D. Sun, and U. X. Tan, "Towards a multi-DOF passive balancing mechanism for upper limbs," in *Proc. IEEE Int. Conf. Rehabil. Robot. (ICORR)*, Aug. 2015, pp. 508–513.

[16] G. Radaelli and J. L. Herder, "Isogeometric shape optimization for compliant mechanisms with prescribed load paths," in *Proc. ASME Int. Design Eng. Tech. Conf. Comput. Inf. Eng. (DETC)*, vol. 5A, 2014, p. 11.

[17] G. Radaelli and J. L. Herder, "A monolithic compliant large-range gravity balancer," *Mech. Mach. Theory*, vol. 102, pp. 55–67, Aug. 2016.

[18] G. Radaelli and J. L. Herder, "Shape optimization and sensitivity of compliant beams for prescribed load-displacement response," *Mech. Sci.*, vol. 7, no. 2, pp. 219–232, 2016.

[19] J. B. Jonker and J. P. Meijaard, "SPACAR—Computer program for dynamic analysis of flexible spatial mechanisms and manipulators," in *Multibody Systems Handbook*, W. Schiehlen, Ed. Heidelberg, Germany: Springer, 1990, pp. 123–143.

[20] J. P. Meijaard, "Fluid-conveying flexible pipes modeled by large-deflection finite elements in multibody systems," *J. Comput. Nonlin. Dyn.*, vol. 9, no. 1, pp. 1415–1555, 2014.

[21] (Mar. 2010). *PA 2200 Performance 1.0 (PA12) EOS GmbH—Electro Optical Systems*. [Online]. Available: https://eos.materialdatacenter.com/eo/material/pdf/30963/PA2200Performance1.0

[22] (Jul. 2004). *Feinpolyamide PA 2200 for EOSINT P EOS GmbH—Electro Optical Systems*. [Online]. Available: https://materflow.com/wp-content/uploads/2018/07/material-data-pa2200.pdf

Martin Tschiersky received the B.Sc. and M.Sc. degrees in mechanical engineering from the University of Duisburg–Essen, Duisburg, Germany, in 2012 and 2014, respectively. He is currently pursuing the Ph.D. degree in mechanical engineering at the University of Twente, Enschede, The Netherlands.

His research interests include the development of assistive and prosthetic devices, passive gravity balancing by means of elastic energy storage and design of flexure-based compliant mechanisms.

Edsko E. G. Hekman (M'18) received the B.Sc. degree in science and engineering from Calvin College, Grand Rapids, MI, USA, in 1981, and the M.Sc. degree in mechanical engineering from the Delft University of Technology, Delft, The Netherlands, in 1986.

After six years of developing equipment for medical research with Radboud University, Nijmegen, he joined the Research and Teaching Staff of the University of Twente, Enschede, The Netherlands. His main research interests are the development of prosthetic, orthotic and robotic devices for restoration of gait and mobility, and in general devices in the technical biomedical field.

Mr. Hekman is a member of the International Society of Biomechanics.

Dannis M. Brouwer received the M.Sc. degree in mechanical engineering in 1998, the P.D.Eng. degree in mechatronic design from the Eindhoven University of Technology, Eindhoven, The Netherlands, in 2001, and the Ph.D. degree from the University of Twente, Enschede, The Netherlands, in 2007.

He has eight years of industrial experience with the Philips Centre for Industrial Technology, Eindhoven, and Demcon Advanced Mechatronics, Enschede. He is currently a Full Professor with the University of Twente, where he acts as the Chair of the Precision Engineering Group and as the Vice Head of the Department of Mechanics of Solids Surfaces and Systems. He has (co)authored over 40 refereed journal articles, 90 conference contributions, and 8 patents on a variety of subjects, including flexure mechanisms, macro and micro manipulators, variable impedance robotics, and precision engineering.

Prof. Brouwer was a recipient of the prestigious personal VIDI Grant for his large range of motion flexure research in 2015, where he was ranked first out of 48 competitors. He has served as the Director-at-Large for the American Society for Precision Engineering and an Associate Editor for *Precision Engineering*.

Just L. Herder (M'06) received the M.Sc. and Ph.D. degrees in mechanical engineering from the Delft University of Technology, Delft, The Netherlands, in 1992 and 2001, respectively.

He held visiting positions with Laval University, Canada, and MIT, USA, as a Fulbright Visiting Scholar. He is currently a Full Professor and the Head of the Precision and Microsystems Department, Delft University of Technology. He has widely published in international peer-reviewed journals and conferences. He holds 25 patents in different areas of mechanism design, based on which seven start-up companies have emerged.

Prof. Herder was a recipient of several international awards, including six Best Paper Awards. He is an ASME Fellow, an Associate Editor of *Mechanism and Machine Theory*, and the Founding Editor-in-Chief of *Mechanical Sciences*. He has given over a dozen keynote talks at international conferences.